Time domain dynamic response functions of elastically anisotropic solids

A. G. Every and K. Y. Kim

Citation: The Journal of the Acoustical Society of America **95**, 2505 (1994); doi: 10.1121/1.409860
View online: https://doi.org/10.1121/1.409860
View Table of Contents: https://asa.scitation.org/toc/jas/95/5
Published by the Acoustical Society of America

Time domain dynamic response functions of elastically anisotropic solids

A. G. Every
Physics Department, University of the Witwatersrand, P.O. Wits 2050, South Africa

K. Y. Kim
Department of Theoretical and Applied Mechanics, Cornell University, Ithaca, New York 14853

(Received 15 September 1993; accepted for publication 15 December 1993)

A method is described for calculating the displacement response function tensor for an infinite anisotropic elastic continuum subjected to a concentrated point force with Heaviside step function time dependence, and examples of computed response functions for zinc, diamond, and silicon are provided. Particular attention is given to the singularities of various orders that travel outward from the point of excitation on the wave surface. The commonly occurring forms that these wave arrival singularities take are described, and explanation provided of how they arise. Some of the singularity types mentioned here have not previously been noted in the literature. Computed response functions for silicon and zinc are compared with waveforms measured in these crystals using the capillary fracture technique.

PACS numbers: 43.35.Cg

INTRODUCTION

The dynamic response functions of elastically anisotropic solids are of interest in many fields including crystal acoustics, solid state physics, nondestructive testing, materials characterization, seismology, applied mechanics, and mathematics. Important general properties of these response functions have been found in the past, but there are only a few situations for which analytical closed form solutions exist, and numerical methods and approximations play an important role in the interpretation of experimental data. Asymptotic far-field solutions are the underpinning of ray acoustics, which is widely used in the interpretation of phonon images[1] and other such phenomena where the wavelengths of the acoustic waves or phonons are very short in comparison with the propagation distances. Phonon images are dominated by the presence of caustics in the energy flux, which is essentially a far-field phenomenon. Recently a number of ultrasonic experiments have been reported[2–9] in which the far-field condition is not as well satisfied, and their interpretation has required going beyond the ray approximation. Some of these experiments have involved ultrasonic tone bursts or the examination of individual Fourier components of more complex signals. In the spatial variation of the signals the broad overall appearance of the focusing pattern is preserved, but the caustics are broadened into an overlapping pattern of diffraction fringes and lose their individual identity. The general features of these diffraction patterns are well accounted for on the basis of computed frequency domain dynamic Green's functions.[5,8]

There are a number of experiments that have recently been performed or are in progress, which examine the response of anisotropic solids to impulsive forces or forces with step function time dependence. These make use of techniques such as capillary fracture and laser excitation to produce the concentrated force or combination of force couples. The interpretation of these experiments requires the computation of the time domain dynamic response functions for the media being studied.

The purpose of this paper is to describe a method for calculating the dynamic response of an infinite anisotropic elastic continuum of general symmetry to a concentrated point force having Heaviside step function time dependence. The dynamic Green's function tensor, i.e., the response to an impulsive force, may be obtained by differentiating the dynamic response with respect to time. Much of the emphasis of this paper is on the singularities, or sharp features, that appear in these response functions, and on providing an explanation for how they arise. These singularities are located on the wave surface and propagate outward at group velocity from the point of excitation and are known as wave arrivals. The surface consists of three sheets, the inner two of which may be folded, and the number of wave arrivals in a particular medium and direction could be as high as 75 (see Ref. 10). Many of the characteristic singularities that occur have been identified previously in the literature, but some are reported here for the first time. Through a number of numerical examples we illustrate the presence of these various singular features in the response functions of actual materials. These singularities survive in the dynamic response functions of elastic half spaces, plates and other bounded geometries, being augmented there by singularities at wave fronts pertaining to various reflection and mode conversion sequences and head waves. The response functions presented here thus provide the basis for at least a partial interpretation of data measured on finite test specimens. In Sec. IV we compare computed response functions for silicon and zinc with

 0001-4966/94/95(5)/2505/12/$6.00

waveforms measured in these crystals using the capillary fracture technique. Prior to the arrival of reflected waves, and within the angular range where head wave effects are not pronounced, there is good agreement between theory and experiment.

I. DYNAMIC RESPONSE FUNCTION TENSOR

We consider here the displacement response $\tilde{G}_{sp}(\mathbf{x},t)$ at point $\mathbf{x}$ and time t of an infinite anisotropic elastic continuum subjected at the origin to a concentrated point force with Heaviside step function time dependence

$$\Theta(t)=\begin{cases}0, & t<0,\\ 1, & t>0.\end{cases} \tag{1}$$

The governing equation for $\tilde{G}_{sp}(\mathbf{x},t)$ is

$$\left(\rho\delta_{rs}\frac{\partial^2}{\partial t^2}-C_{rlsm}\frac{\partial^2}{\partial x_l\partial x_m}\right)\tilde{G}_{sp}(\mathbf{x},t)=\delta_{rp}\delta(\mathbf{x})\Theta(t), \tag{2}$$

where ρ is the density and C_{rlsm} is the elastic stiffness tensor for the medium, and s and p refer to the sensing and forcing directions, respectively. The components of $\tilde{G}_{sp}(\mathbf{x},t)$ transform as a second rank tensor. The application of integral transforms to this and related Green's function equations is well documented.[10–22] The approach we take here follows closely on that used in Ref. 8, in which we have treated the frequency domain Green's function. On carrying out a quadruple space-time Fourier transform on Eq. (2) we obtain

$$L_{rs}(\mathbf{k},\omega)\tilde{g}_{sp}(\mathbf{k},\omega)=[1/(2\pi)^3]\delta_{rp}f(\omega), \tag{3}$$

where

$$L_{rs}(\mathbf{k},\omega)=C_{rlsm}k_lk_m-\rho\omega^2\delta_{rs}, \tag{4}$$

and $f(\omega)=-1/2\pi i\omega+\delta(\omega)/2$ is the Fourier transform of $\Theta(t)$. On solving Eq. (3) and carrying out the inverse Fourier transform we obtain

$$\tilde{G}_{sp}(\mathbf{x},t)=\int_{-\infty}^{\infty}G_{sp}(\mathbf{x},\omega)f(\omega)e^{-i\omega t}\,d\omega, \tag{5}$$

where

$$G_{sp}(\mathbf{x},\omega)=\frac{1}{(2\pi)^3}\int d^3\mathbf{k}[L^{-1}(\mathbf{k},\omega)]_{sp}e^{i\mathbf{k}\cdot\mathbf{x}} \tag{6}$$

is the frequency domain Green's function for the medium. Using the spectral resolution theorem,[16] we can write

$$(L^{-1})_{sp}=\sum_{j=1}^{3}\frac{\Lambda_{sp}^{(j)}}{\rho v^{(j)2}k^2-\rho\omega^2}=\sum_{j=1}^{3}\frac{s^{(j)2}\Lambda_{sp}^{(j)}}{\rho(k^2-\omega^2s^{(j)2})}, \tag{7}$$

where the sum is taken over the three eigenvalues $\rho v^{(j)2}k^2$ of the tensor $\Gamma_{rs}=C_{rlsm}k_lk_m$, $v^{(j)}$ is the phase velocity and $s^{(j)}=1/v^{(j)}$ the slowness, and $\Lambda_{sp}^{(j)}=U_s^{(j)}U_p^{(j)}$, where $\mathbf{U}^{(j)}$ is the eigenvector associated with $\rho v^{(j)2}k^2$. In performing the integration in Eq. (6) it is convenient to orient the k_3 axis in the direction of $\mathbf{x}$ and transform to polar coordinates so that $\mathbf{k}=k(\sin\theta\cos\phi,\ \sin\theta\sin\phi,\ \cos\theta)$ and $d^3\mathbf{k}\rightarrow d\Omega\,k^2\,dk$, where $d\Omega=d(\cos\theta)d\phi$ is the element of solid angle in k space. Integration with respect to k is facilitated by taking the limits to be $-\infty$ to ∞ rather than 0 to ∞, and to compensate, the angular integral is taken only over the forward unit hemisphere for which $\cos\theta\geqslant 0$, rather than over the entire sphere. The poles that are encountered in the k integral are handled by ascribing a small positive imaginary part $i\epsilon$ to ω, corresponding to the slow switching on of the force. The path of integration is then completed in the upper or lower half complex plane depending on the sign of $x\cos\theta$. This leads to the result

$$G_{sp}(\mathbf{x},\omega)=\sum_{j=1}^{3}\left[\frac{i\omega}{8\pi^2\rho}\int_{\cap}d\Omega\,s^{(j)3}\Lambda_{sp}^{(j)}e^{i\omega s^{(j)}\cdot\mathbf{x}}+\frac{1}{8\pi^2\rho x}\int_0^{2\pi}d\phi\,s^{(j)2}\Lambda_{sp}^{(j)}\right]. \tag{8}$$

The first term is a surface integral taken over the forward hemisphere, and the second one is a line integral taken around the periphery of this hemisphere. The factor $\Lambda_{sp}^{(j)}=U_s^{(j)}U_p^{(j)}$ represents the weighting for each plane wave contributing to $G_{sp}(\mathbf{x},\omega)$, and depends on the projection of the polarization vector of that wave on the sensing and forcing directions.

On combining Eqs. (5) and (8) and integrating with respect to time one obtains the corresponding expression for the time domain response function

$$\tilde{G}_{sp}(\mathbf{x},t)=\sum_{j=1}^{3}\left[\frac{-1}{8\pi^2\rho}\int_{\cap}d\Omega\,s^{(j)3}\Lambda_{sp}^{(j)}\delta(t-\mathbf{s}^{(j)}\cdot\mathbf{x})+\frac{\Theta(t)}{8\pi^2\rho x}\int_0^{2\pi}d\phi\,s^{(j)2}\Lambda_{sp}^{(j)}\right]. \tag{9}$$

We have used Fourier transforms in deriving Eq. (9) for consistency with the related study we have undertaken in Ref. 8, but it should be pointed out that there are other more direct methods of arriving at this result. One such is to proceed from Eq. (4.6) of Burridge[14] which expresses the Green's function, i.e., response to a $\delta(t)$ force, as an integral over the sphere, and in which the generalized distribution function $\delta'(t-\mathbf{s}^{(j)}\cdot\mathbf{x})$ appears in the integrand. Burridge's expression, as it stands, is not very suitable for numerical computations, and it is advantageous to integrate it, with respect to time, to obtain $\tilde{G}_{sp}(\mathbf{x},t)$. Integrating by parts yields two terms, a line integral, which is the second term in Eq. (9), and a surface integral over the unit sphere, which on dropping the integral over the second hemisphere which is zero, becomes the first term in Eq. (9). Yeatts[16] has derived a similar result to that of Burridge, but more general, using Radon transforms.

There are only a few special cases for which closed form solutions for the integrals in Eq. (8) are known, notably for isotropic media,[23,24] along the zonal axis of transversely isotropic media[11] and for certain special values of the elastic constants which lead to uncoupling of the equations of motion and render the slowness surface in the form of three concentric ellipsoids.[25,26] Barring these special cases, the integrals in Eq. (9) require numerical methods for their evaluation.

The first term in Eq. (9), because it involves 2-D integration, is the most CPU intensive. The properties of the

δ function could be used to reduce this surface integral to a line integral summed over directions for which $t-\mathbf{s}^{(j)}\cdot\mathbf{x}=0$, which have to be located numerically. However, there is no clear-cut advantage to doing this when it is the entire time dependence of $\tilde{G}_{sp}(\mathbf{x},t)$ that is being sought. In this case it is simpler, and not necessarily more demanding on computer time, to perform the 2-D integration as a sorting and counting process. The time interval between $t=0$ and the arrival of the last wave, i.e., the largest value of $\mathbf{s}^{(j)}\cdot\mathbf{x}$, is divided into N slots, which in our calculations has been taken to be 240. A rectangular grid of $\cos\theta$, ϕ points is chosen, and for each one the value of $\mathbf{s}^{(j)}\cdot\mathbf{x}$ determines the slot in which the corresponding value of $s^{(j)3}\Lambda_{sp}^{(j)}$ is accumulated. Typically we find that by taking a 2000×2000 grid of points the noise level in the results is reduced to an acceptable value; the singularities are sharply defined and $\tilde{G}$ is reasonably smooth to the eye at other times (a finer grid of points is required to achieve the same quality on a finer time scale). The computational time for such a calculation on an IBM3083 computer is of the order of 5 to 10 min. From a mathematical point of view this procedure is analogous to determining the frequency distribution function for the vibrations of a two-dimensional lattice. The analogy is an apt one, since here too there occur van Hove type singularities.[27] These are discussed in the next section. For times exceeding the maximum of all the $\mathbf{s}^{(j)}\cdot\mathbf{x}$, $\tilde{G}_{sp}(\mathbf{x},t)$ has the constant value given by the second term in Eq. (9), which is the static Green's function of the medium. This second term is equivalent to the expression given by Barnett[28] for the static Green's function. At these later times the response to an impulsive force, obtained by differentiating $\tilde{G}_{sp}(\mathbf{x},t)$ with respect to t, is zero, representing a lacuna in the Green's function.[10]

II. WAVE ARRIVAL SINGULARITIES

Singularities in the time dependence of $\tilde{G}_{sp}(\mathbf{x},t)$ occur for points on the slowness surface where $\mathbf{s}^{(j)}\cdot\mathbf{x}$ is stationary, and this for fairly obvious geometrical reasons is where the outward normal to the slowness surface, or ray vector, is parallel to $\mathbf{x}$. These singularities propagate outward from the source at group velocity $\mathbf{V}$ in any direction, and are known as wave arrivals. Collectively they lie on the wave surface, which is the group velocity surface scaled in size by a factor t. There are a number of different singular forms that these wave arrivals can take, depending on whether the associated point (or points) on the slowness surface is generic or not, what the curvature of the slowness surface there is, and whether the point lies in a symmetry direction or not. In symmetry directions different components of the response function tensor may exhibit different singular forms. The behaviour of $\tilde{G}_{sp}(\mathbf{x},t)$ in the immediate vicinity of a wave arrival is found by approximating the equation of the slowness surface and if necessary also Λ_{rs} as a low-order polynomial and carrying out the integration analytically. Listed below are the more common forms that these singularities can take, together with some explanation of the way they arise. Examples of typical computed response functions exhibiting these singularities are provided in the following section. The line integral in Eq. (9) is not considered here since it is a constant and does not contribute to the singular behavior.

A. Elliptic points on the slowness surface

The slowness surface is said to be elliptic when it is either convex or concave, i.e., both principal curvatures are of the same sign. The nature of the singular behavior for generic points of this type is the same for all components of $\tilde{G}_{sp}(\mathbf{x},t)$ and does not depend on which branch of the wave surface (longitudinal, slow transverse or fast transverse) the wave arrival is associated with. For the purpose of discussion we may therefore suppress the indices sp and j. We consider the singular behavior of $\tilde{G}(\mathbf{x},t)$ close to the time t_0 of the wave arrival associated with the point $\mathbf{s}_0$ on the slowness surface. The singularity propagates outwards at group velocity $\mathbf{V}=\mathbf{x}/t_0$, which is normal to the slowness surface at $\mathbf{s}_0$. From the polar reciprocal relationship between $\mathbf{s}_0$ and $\mathbf{V}$, $\mathbf{s}_0\cdot\mathbf{V}=sV\cos\psi=1$, where ψ is the angle between $\mathbf{s}_0$ and $\mathbf{V}$. The singular behavior of $\tilde{G}(\mathbf{x},t)$ is determined by the shape of the slowness surface in the immediate vicinity of $\mathbf{s}_0$, and confining the surface integral in Eq. (8) to a small region around that point. In a local system of coordinates with origin located at $\mathbf{s}_0$, s_3 taken normal to the slowness surface (i.e., in the direction of $\mathbf{x}$) and s_1 and s_2 pointing in the directions of principal curvature of the slowness surface, we have that $d\Omega\approx ds_1\,ds_2\cos\psi/s_0^2=ds_1\,ds_2(Vs_0^3)^{-1}$, $s^3\approx s_0^3$, $\Lambda\approx$constant, $s_3=-(\alpha s_1^2+\beta s_2^2)+\cdots$, where 2α and 2β are the two principal curvatures of the slowness surface (both positive if the surface is convex or both negative if the surface is concave), and $\mathbf{s}\cdot\mathbf{x}=\mathbf{s}_0\cdot\mathbf{x}+s_3x$, where $x=|\mathbf{x}|$. Hence, $\mathbf{s}\cdot\mathbf{x}=\mathbf{s}_0\cdot\mathbf{V}t_0-(\alpha s_1^2+\beta s_2^2)x=t_0-(\alpha s_1^2+\beta s_2^2)x$. The singular behavior of $\tilde{G}(\mathbf{x},t)$ therefore derives from an integral of the form

$$\tilde{G}(\mathbf{x},T)=-F\Lambda\int ds_1\,ds_2\,\delta(T+[\alpha s_1^2+\beta s_2^2]x), \quad (10)$$

where $T=t-t_0$ and $F=(8\pi^2\rho V)^{-1}$. For T the same sign as α and β, $\tilde{G}(\mathbf{x},t)=0$. For T opposite in sign to α and β we proceed as follows. On substituting $s_1=\alpha^{-1/2}x^{-1/2}u$ and $s_2=\beta^{-1/2}x^{-1/2}v$ we obtain

$$\tilde{G}(\mathbf{x},T)=\frac{-F\Lambda}{\sqrt{\alpha\beta}x}\int du\,dv\,\delta(-|T|+u^2+v^2). \quad (11)$$

The integration with respect to u is carried out by making use of the identity

$$\delta(f(u))=\sum_i\left|\frac{\partial f}{\partial u}\right|_i^{-1}, \quad (12)$$

where the derivatives are evaluated at the roots of $f(u)=0$ to yield, after substituting $v=|T|^{1/2}y$ and integrating with respect to y

$$\tilde{G}(\mathbf{x},T)=\frac{-F\Lambda\pi}{\sqrt{\alpha\beta}x}\begin{cases}\Theta(-T), & \alpha,\beta>0,\\ \Theta(T), & \alpha,\beta<0.\end{cases} \quad (13)$$

Thus $\tilde{G}(\mathbf{x},T)$ exhibits a discontinuity or jump at $T=0$. The sign of the jump for the diagonal components of $\tilde{G}_{sp}(\mathbf{x},T)$ is the same as that of α and β, since for those components $\Lambda>0$, whereas for the off-diagonal components the jump may be of either sign. The magnitude of the discontinuity is inversely proportional to the square root of $K=4\alpha\beta$, the Gaussian curvature of the slowness surface. This result is linked to the phenomenon of phonon focusing,[1,29] whereby the energy flux radiated from a point source in the ray approximation is inversely proportional to K. The discontinuity is essentially a far-field effect, being dominated by high-frequency Fourier components of the response, and falling off inversely with the first power of distance. Near lines of zero Gaussian curvature on the slowness surface the magnitude of the discontinuity becomes very large, and a higher order approximation for the equation of the slowness surface is required, as discussed below. Likewise, if the forcing or sensing direction is perpendicular to the polarization vector for $\mathbf{s}_0$, or nearly so, then $|\Lambda|\ll 1$ and the discontinuity is very small, and an expansion for $\Lambda(\mathbf{s})$ is required in order to arrive at a more accurate description of the singular behavior. The way this arises in the presence of symmetry is discussed later.

B. Hyperbolic points on the slowness surface

When one of the principal curvatures, say 2α, is negative and the other one positive the slowness surface is saddle shaped and said to be hyperbolic. Following a similar procedure to that outlined above, on integrating with respect to u one arrives, for $T>0$, at

$$\tilde{G}(\mathbf{x},T)=\frac{-F\Lambda}{\sqrt{-\alpha\beta x}}\int\frac{dv}{\sqrt{T+v^2}}, \tag{14}$$

where the limits of the integral over v are taken large but not infinite to avoid an unphysical divergence. The integral evaluates approximately to $-\ln(T)+$ a constant. For $T<0$ the same result is obtained by replacing T by $-T$, and it follows therefore that, near $T=0$, $\tilde{G}(\mathbf{x},T)$ exhibits a logarithmic divergence given by

$$\tilde{G}(\mathbf{x},T)=\frac{F\Lambda\ln(|T|)}{\sqrt{-\alpha\beta x}}. \tag{15}$$

The above results for elliptic and hyperbolic points have been noted in a number of papers in the past, including Buchwald,[13] Burridge,[14] and Cameron and Eason,[15] and are discussed in detail in the book by Payton.[11] We have repeated the derivations here to establish the method by which some of the previously undisclosed results discussed below are obtained.

C. Elliptic and hyperbolic points in a symmetry plane

For $\mathbf{s}_0$ lying in a mirror symmetry plane of the medium, but not on an acoustic axis, $\mathbf{x}$ lies in this plane as well, and the polarization vector $\mathbf{U}(\mathbf{s}_0)$ is located either in or perpendicular to this plane. Let the coordinate frame to which $\mathbf{x}$, $\tilde{G}_{sp}(\mathbf{x},t)$ and $\mathbf{U}$ are referred be located such that x_1 and x_3 lie in the plane and x_2 is perpendicular to the plane. On symmetry grounds $\tilde{G}_{12}=\tilde{G}_{21}=\tilde{G}_{32}=\tilde{G}_{23}\equiv 0$. For the pure transverse mode $\mathbf{U}(\mathbf{s}_0)=(0,1,0)$ and $\Lambda_{11}(\mathbf{s}_0)=\Lambda_{33}(\mathbf{s}_0)=\Lambda_{13}(\mathbf{s}_0)=\Lambda_{31}(\mathbf{s}_0)\equiv 0$, and as a result the corresponding components of $\tilde{G}_{sp}$ (but not $\tilde{G}_{22}$) display at the wave arrival not a discontinuity, but a lower order singularity. To ascertain the form of this singularity we expand $\Lambda(\mathbf{s})$ in powers of s_1 and s_2, with s_3 as usual being in the direction of $\mathbf{x}$. On symmetry grounds the directions of principal curvature are in and perpendicular to the symmetry plane and in addition the weighting factor takes on the simple form $\Lambda(\mathbf{s})=as_2^2+\cdots$, where a is a constant. For a mode that is polarized in the symmetry plane, it is $\Lambda_{22}(\mathbf{s})$ instead that is expanded and thus $\tilde{G}_{22}$ that exhibits the lower order singularity.

For convex or concave slowness surface we have

$$\tilde{G}(\mathbf{x},T)=-Fa\int ds_1\,ds_2\,s_2^2\delta(T+[\alpha s_1^2+\beta s_2^2]x). \tag{16}$$

For T having the same sign as that of α and β, $\tilde{G}(\mathbf{x},t)=0$. For T opposite in sign to α and β Eq. (15) becomes, on substituting $s_1=\alpha^{-1/2}x^{-1/2}u$ and $s_2=\beta^{-1/2}x^{-1/2}v$,

$$\tilde{G}(\mathbf{x},T)=\frac{-Fa}{\sqrt{\alpha\beta^3x^2}}\int du\,dv\,v^2\delta(-|T|+u^2+v^2), \tag{17}$$

and hence

$$\tilde{G}(\mathbf{x},T)=\frac{-Fa}{\sqrt{\alpha\beta^3x^2}}\int_{-\sqrt{|T|}}^{\sqrt{|T|}}\frac{dv\,v^2}{\sqrt{|T|-v^2}}. \tag{18}$$

The integral evaluates to $(\pi/2)|T|$ and thus the singular behavior takes the form

$$\tilde{G}(\mathbf{x},T)=\frac{-Fa\pi}{2\sqrt{\alpha\beta^3x^2}}\begin{cases}|T|\Theta(-T), & \alpha,\beta>0,\\ |T|\Theta(T), & \alpha,\beta<0.\end{cases} \tag{19}$$

Thus $\tilde{G}(\mathbf{x},T)$ is continuous but has a kink, i.e., its time derivative $\partial\tilde{G}/\partial T$ exhibits a discontinuity at $T=0$. The magnitude of this discontinuity falls off with distance as $1/x^2$, characterizing this as a near-field effect. A simple explanation for the $1/x^2$ dependence is that $\tilde{G}(\mathbf{x},T)$ scales inversely with x, and t_0 scales linearly with x, and therefore on dimensional grounds $\partial\tilde{G}/\partial T$ scales as $1/x^2$. Similar analysis, when the slowness surface is saddle shaped, shows that $\tilde{G}(\mathbf{x},T)$ is continuous but its time derivative exhibits a logarithmic divergence given by

$$\frac{\partial\tilde{G}(\mathbf{x},T)}{\partial T}=\frac{-Fa\ln|T|}{2\sqrt{-\alpha\beta^3x^2}}. \tag{20}$$

If the wave surface happens to be folded, which is a common feature of anisotropic solids, there may be one or more wave arrival in a symmetry plane which is associated with an $\mathbf{s}_0$ that does not lie in that plane. The corresponding mode is thus unlikely to be polarized either in or perpendicular to the symmetry plane, and in general therefore all the components of $\tilde{G}_{sp}$ will display the same jump or logarithmic singularity.

D. The pure transverse mode in transversely isotropic media

In hexagonal crystals and other transversely isotropic elastic solids, for any direction of propagation there is one pure transverse mode, polarized in the plane normal to the principal symmetry axis. With the x_3 axis located along this symmetry axis, it follows that for the pure transverse mode $\Lambda_{33}=\Lambda_{31}=\Lambda_{13}=\Lambda_{32}=\Lambda_{23}\equiv 0$ for *all* s. Therefore the pure transverse mode does not contribute at all to the components $\tilde{G}_{33}$, $\tilde{G}_{31}$, $\tilde{G}_{13}$, $\tilde{G}_{32}$, and $\tilde{G}_{23}$ of the response function, and consequently there is no singularity at all for these components at the wave arrival. Since all planes containing the x_3 axis are equivalent symmetry planes, one may with no loss of generality locate the x_1 axis in the plane containing **x**. It follows that $\tilde{G}_{12}=\tilde{G}_{21}=\tilde{G}_{32}=\tilde{G}_{23}\equiv 0$, $\tilde{G}_{22}$ exhibits a discontinuity while $\tilde{G}_{11}$ displays a kink at the pure transverse wave arrival.

Near to fourfold symmetry axes in cubic and tetragonal media, in certain elastic constant ranges encompassing isotropy, the polarization patterns for the two transverse modes resemble very closely those of the transverse (T) and quasitransverse (qT) modes in transverse isotropy, being approximately radial and circumferential with respect to the symmetry axis.[30] The conditions on $\tilde{G}_{sp}$ obtained above therefore to a good approximation hold also for those media. This is the underlying reason why, for instance, the fast transverse (FT) modes are not in evidence in the laser-generated results of Every *et al.*[2,3] on ⟨100⟩ oriented silicon.

E. Parabolic points on the slowness surface

Lines of zero curvature on the slowness surface, known as parabolic lines, correspond to folds (cuspidal edges) in the wave surface, and in the ray approximation to line caustics in the energy flux.[1] On the inside of the fold there are two closely spaced wave arrivals corresponding to points $\mathbf{s}_a$ and $\mathbf{s}_b$ on either side of the parabolic line where the slowness surface is saddle shaped and convex (or concave), respectively. As the fold is approached, the Gaussian curvatures at $\mathbf{s}_a$ and $\mathbf{s}_b$ tend to zero and so the magnitudes of the discontinuity and logarithmic divergence grow very large and these singularities arrive progressively closer in time. Precisely at the fold, there is only one wave arrival carrying with it a singularity of higher order. For a generic point $\mathbf{s}_0$ on the parabolic line (where $\mathbf{s}_a$ and $\mathbf{s}_b$ meet), one of the principal curvatures, say 2β, is zero. There is no loss of generality if we take $\alpha>0$. The power series expansion for the slowness surface must now be taken to higher order in s_2, and it is sufficient[13,31] to take it as $s_3=-(\alpha s_1^2+\gamma s_2^3)+\cdots$, where γ is a positive constant (the direction of s_2 is chosen to make it so). The singular behavior of $\tilde{G}(\mathbf{x},T)$ is thus given by

$$\tilde{G}(\mathbf{x},T)=-F\Lambda\int ds_1\,ds_2\,\delta(T+[\alpha s_1^2+\gamma s_2^3]x). \quad (21)$$

On substituting $s_1=\alpha^{-1/2}x^{-1/2}u$ and $s_2=\gamma^{-1/3}x^{-1/3}v$ we obtain

$$\tilde{G}(\mathbf{x},T)=\frac{-F\Lambda}{\alpha^{1/2}\gamma^{1/3}x^{5/6}}\int du\,dv\,\delta(T+u^2+v^3), \quad (22)$$

which on carrying out the integration yields

$$\tilde{G}(\mathbf{x},T)=\frac{-F\Lambda g(\mathrm{sgn}(T))}{\alpha^{1/2}\gamma^{1/3}x^{5/6}|T|^{1/6}}, \quad (23)$$

where $g(+)=2.429$ and $g(-)=4.206$. Thus $\tilde{G}(\mathbf{x},T)$ exhibits a $1/|T|^{1/6}$ divergence at the wave arrival with a $1/x^{5/6}$ dependence on distance characteristic of the wave field at a line caustic.[13] The number $\sigma=\frac{1}{6}$ is known as the singularity index for the fold caustic.[32]

The two sheets of the wave surface terminate at the fold edge, and beyond the edge there is no wave arrival and thus no singular feature in the mathematical sense. Nevertheless, a deep nonsingular minimum persists in $\tilde{G}(\mathbf{x},T)$, falling off as $\sim 1/|\delta x_2|^{1/4}$, where δx_2 is the distance, measured in the direction of s_2, from the point **x** on the cuspidal edge. Such quasisingular features are a common presence in computed response functions, and examples of them can be found in Secs. III and IV.

In symmetry planes, as seen earlier, Λ may vanish and an expansion for Λ is required. The divergence in this case is replaced by a lower order singularity in which $\tilde{G}(\mathbf{x},T)$ is continuous but its time derivative

$$\frac{\partial\tilde{G}(\mathbf{x},T)}{\partial T}=\frac{-F\,ag(\mathrm{sgn}(T))}{2\alpha^{3/2}\gamma^{1/3}x^{11/6}|T|^{1/6}}$$

displays a $1/|T|^{1/6}$ divergence.

F. For x in the direction of a cusp caustic

There are isolated points on a parabolic line where the direction of vanishing principal curvature is parallel to the parabolic line. These map onto cuspidal points on the wave surface where two fold edges meet, and onto cusp caustics in the energy flux. In the region between the folds the particular sheet of the wave surface comprises three cojoined layers and so there are three closely spaced wave arrivals, two carrying discontinuities and the third a logarithmic divergence. At the cuspidal point these all coalesce and give rise to a higher order singularity. Outside the folds there is a single sheet of the wave surface carrying with it a discontinuity or logarithmic divergence, which becomes very large as the cuspidal point is approached.

In the region of the point $\mathbf{s}_0$ on the slowness surface which maps onto the cuspidal point, the equation of the slowness surface takes the form $s_3=-(\alpha s_1^2+\zeta s_1 s_2^2+\epsilon s_2^4)+\cdots$, where α, ζ, and ϵ are constants which can all be taken to be of the same sign. On the line passing through the local origin in the s_1 direction, the change in sign of the principal curvature in the s_2 direction is effected by the second term. The third term restores the convexity (or concavity) for larger s_2 and is associated with the curvature of the parabolic line.

The singular behavior of $\tilde{G}(\mathbf{x},T)$ is thus given by

$$\tilde{G}(\mathbf{x},T)=-F\Lambda\int ds_1\,ds_2\,\delta(T+[\alpha s_1^2+\zeta s_1 s_2^2+\epsilon s_2^4]x), \quad (24)$$

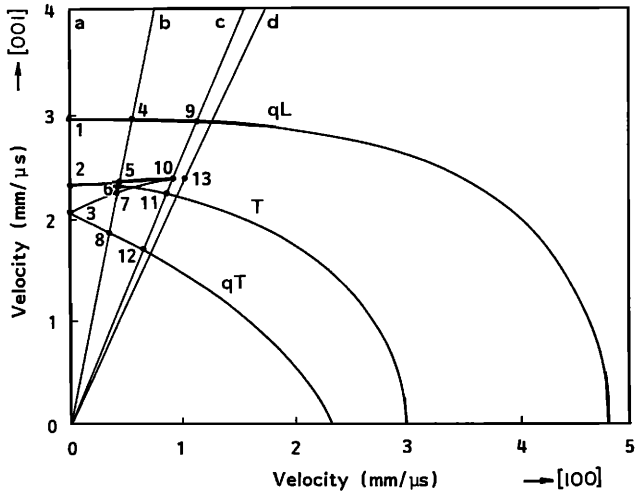

FIG. 1. (a) An (010) section of the ray surface (wave surface for $t=1$) of zinc.

which on substituting $s_1=\alpha^{-1/2}x^{-1/2}u$ and $s_2=\alpha^{1/4}\zeta^{-1/2}x^{-1/4}v$ becomes

$$\tilde{G}(\mathbf{x},T)=\frac{-F\Lambda}{\alpha^{1/4}\zeta^{1/2}x^{3/4}}\int du\,dv\,\delta\left(T+u^2+uv^2+\frac{\epsilon\alpha}{\zeta^2}v^4\right). \tag{25}$$

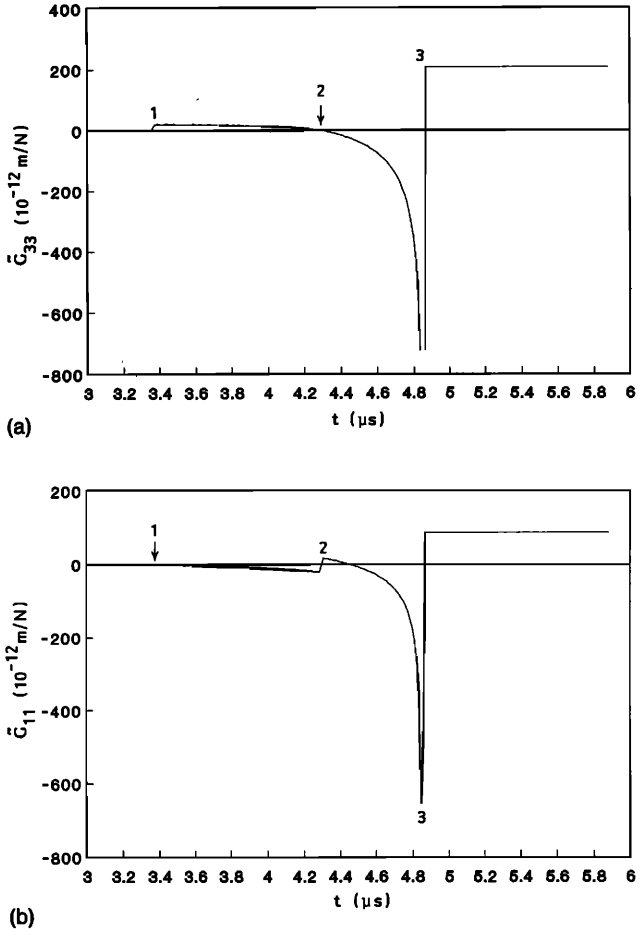

FIG. 2. (a) $\tilde{G}_{33}$ and (b) $\tilde{G}_{11}$ for zinc in direction a along the high symmetry axis. $x=10$ mm.

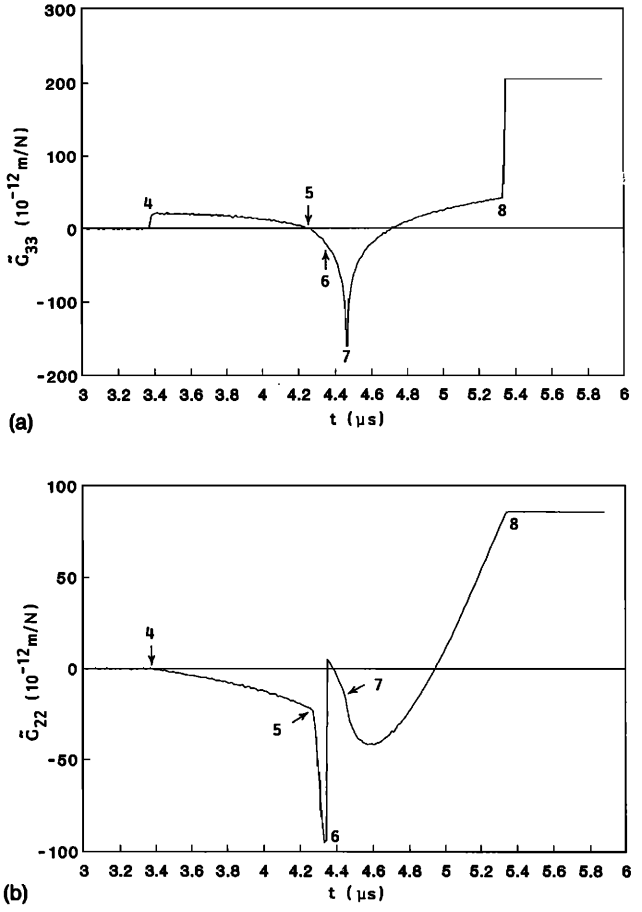

FIG. 3. (a) $\tilde{G}_{33}$ and (b) $\tilde{G}_{22}$ for zinc in direction b. $\mathbf{x}=(2.0,0,10.0)$ in mm.

On carrying out the integration we obtain

$$\tilde{G}(\mathbf{x},T)=\frac{-F\Lambda g(\mathrm{sgn}(\eta),\mathrm{sgn}(T))}{\alpha^{1/4}\zeta^{1/2}|\eta|^{1/4}x^{3/4}|T|^{1/4}}, \tag{26}$$

where $\eta=1/4-\epsilon\alpha/\zeta^2$, $g(+,+)=g(-,-)=2.622$, $g(+,-)=3.708$ and $g(-,+)=0$. Thus $\tilde{G}(\mathbf{x},T)$ exhibits a singularity of the form $1/|T|^{1/4}$ at the wave arrival, with a $1/x^{3/4}$ falloff with distance characteristic of the wave field at a cusp caustic. The singularity index is $\sigma=\frac{1}{4}$ in this case.

Cusp caustics are often to be found on symmetry planes. The reason for this is simple. A parabolic line meets a symmetry plane at right angles, unless that point of intersection happens to coincide with an acoustic axis. Since the direction of vanishing principal curvature there is either in or perpendicular to that plane, it must either be parallel or perpendicular to the parabolic line. In a symmetry plane, for those components of $\tilde{G}(\mathbf{x},T)$ for which $\Lambda=0$, the singularity is softened with $\tilde{G}$ being continuous but its time derivative

$$\frac{\partial\tilde{G}(\mathbf{x},T)}{\partial T}=\frac{-Fa\alpha^{1/4}g_2(\mathrm{sgn}(\eta),\mathrm{sgn}(T))}{\zeta^{3/2}|\eta|^{3/4}x^{5/4}|T|^{3/4}} \tag{27}$$

displaying a $1/|T|^{3/4}$ divergence.

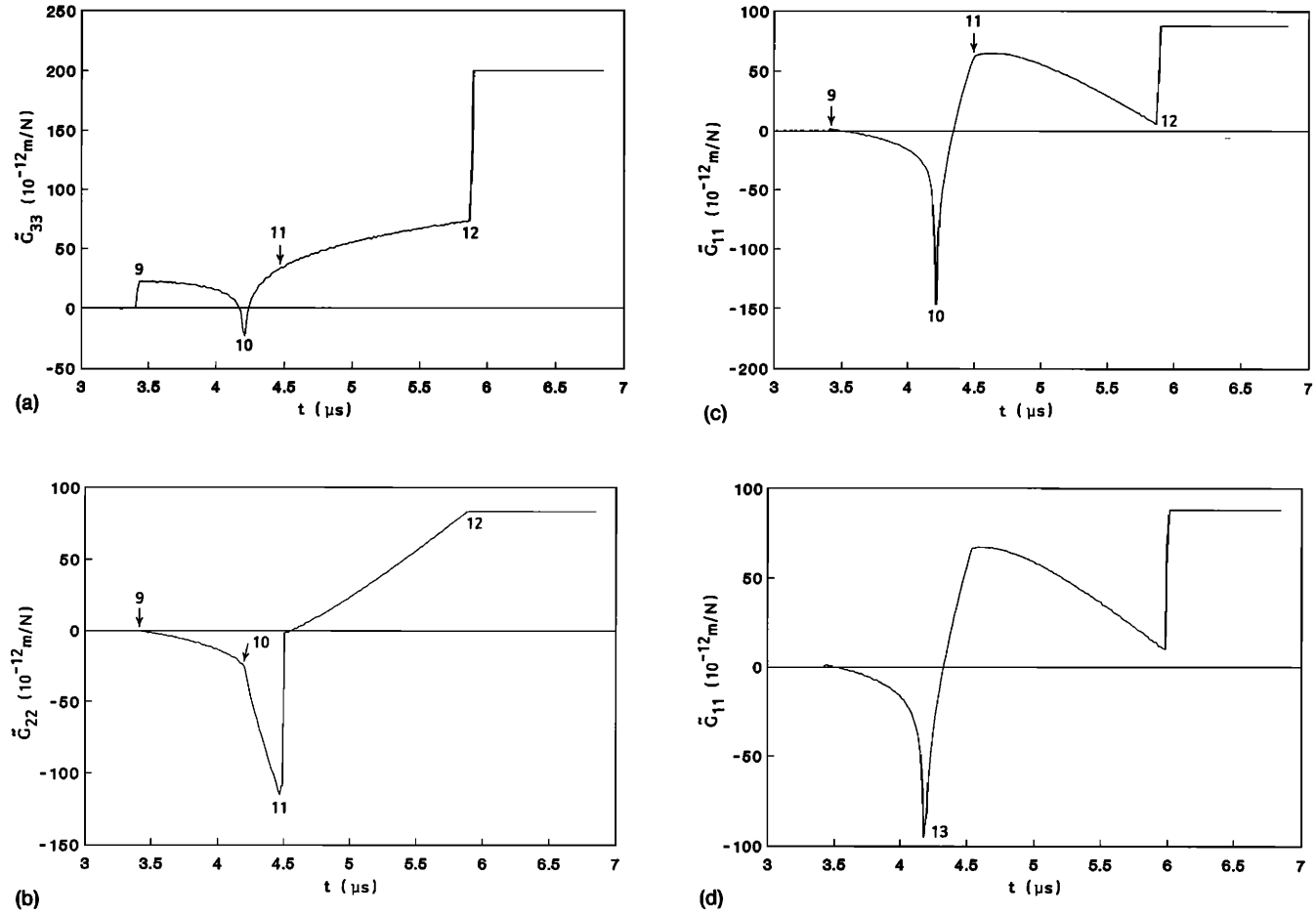

FIG. 4. (a) $\tilde{G}_{33}$, (b) $\tilde{G}_{22}$, (c) $\tilde{G}_{11}$ for zinc in direction c of the fold in the ray surface. $\mathbf{x}=(3.94,0,10.0)$ in mm. (d) $\tilde{G}_{11}$ for direction d, slightly beyond the fold. $\mathbf{x}=(4.3,0,10.0)$ in mm.

G. Conical point in the wave surface

Along the principal symmetry axis of a transversely isotropic solid (or hexagonal crystal) the wave surface possesses a conical point when the elastic constants satisfy the inequality[33]

$$(C_{13}+C_{44})^2/[C_{13}(C_{33}-C_{44})]>1. \tag{28}$$

Under these conditions the quasitransverse sheet of the slowness surface is concave near the symmetry axis. Concentric with this axis are two circular parabolic lines where the surface first changes to saddle shaped and then to convex. The first of these lines maps onto a circular fold in the wave surface (see Fig. 1) and a line caustic in the energy flux. All points on the second parabolic line share a common tangent plane and their surface normals are all parallel to the symmetry axis. This parabolic line maps onto a conical point in the wave surface where a single ray corresponds to a cone of slowness vectors. The associated caustic is thus highly degenerate, comprising the single point on the symmetry axis. Kim *et al.*[7] have observed the intense focusing associated with this caustic in zinc using a number of different ultrasonic techniques. The way this caustic unfolds into a pattern of fold and cusp caustics when the symmetry is lowered, has been described by Every.[33] The form of the singularity at this conical point in the wave surface is discussed in the book by Payton,[11] and is

$$\tilde{G}(\mathbf{x},T)\approx\begin{cases}1/\sqrt{|T|x}, & T<0,\\ 1/x, & T>0.\end{cases} \tag{29}$$

From symmetry, it is only the components $\tilde{G}_{11}=\tilde{G}_{22}$ and $\tilde{G}_{33}$ that are nonzero and display this singularity. The singularity index $\sigma=\frac{1}{2}$ for $T<0$ attests to the high order of this singularity.[13] Away from the symmetry axis there is a splitting into two wave arrivals, the earlier one carrying a logarithmic singularity and the later one a discontinuity.

H. Conical point in the slowness surface

At a point where two sheets of the slowness surface meet in the shape of a cone, the surface normal, and hence, the ray vector is undefined. Burridge[14] has analyzed the singular behavior associated with the conical point in cubic media (there are eight such equivalent points in the ⟨111⟩ directions) and has shown that it extends over a disk, or lid, which is tangential to the neighboring portions of the wave surface. On this lid the Green's function exhibits a discontinuity and so the response function $\tilde{G}(\mathbf{x},T)$ exhibits a kink (change in slope). The magnitude of this kink depends on the particular component of $\tilde{G}_{sp}(\mathbf{x},t)$ and scales as $1/x^2$, and this singularity is thus a near-field effect. The

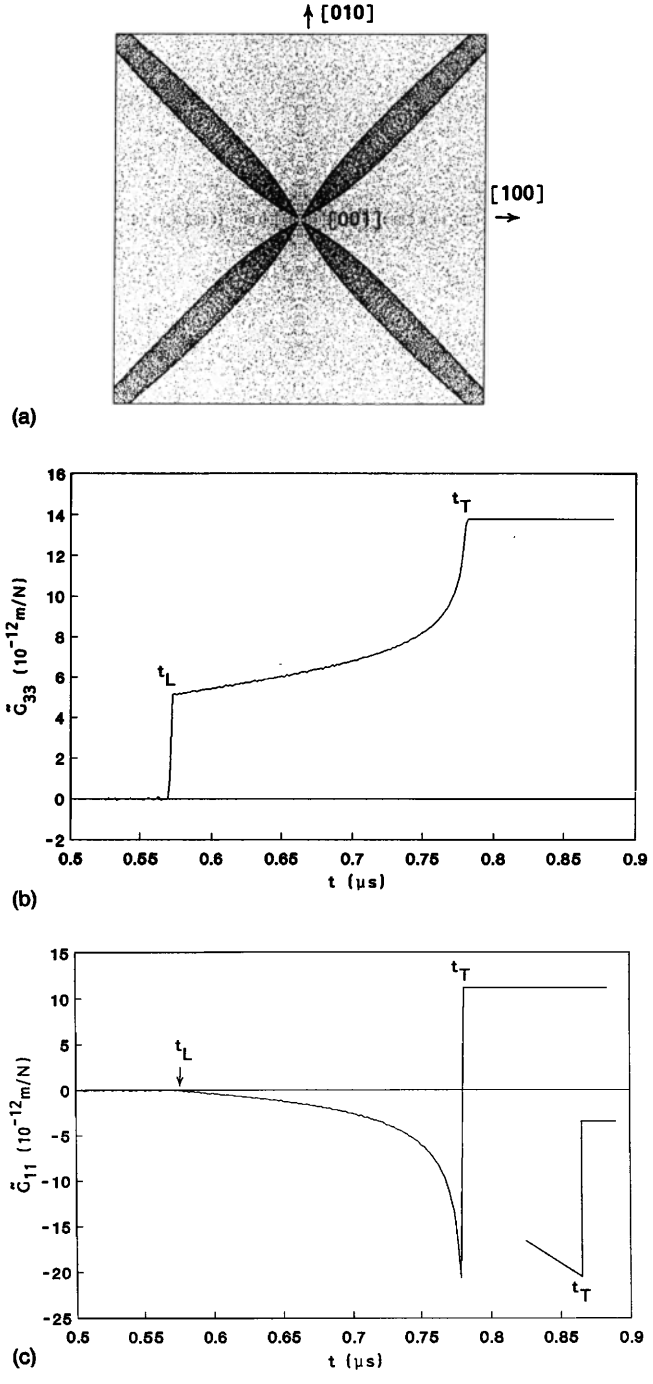

FIG. 5. (a) ST+FT focusing pattern of diamond centered on the [001] direction, with darkness being the measure of intensity. Angular width from left to right is 17°. (b) $\tilde{G}_{33}$ and (c) $\tilde{G}_{11}$ for diamond in the direction of the cube axis. $x=10$ mm. t_L and t_T denote the longitudinal and transverse wave arrivals, respectively. The inset in (c) shows the region of the T arrival on an expanded time scale.

lid is circular and normal to the symmetry axis, and its circumference is the locus of rays associated with points on the slowness surface infinitesimally close to the conical point. Whatever the direction of the force, provided it has a component normal to the axis, it is the displacement component parallel to the lid which exhibits the singular behavior. This is because the modes in the vicinity of the conical point, from which the singularity is derived, are pure transverse. Barry and Musgrave[34] have extended Burridge's results to conical points in tetragonal media.

I. Tangential degeneracies in the slowness surface

Tangential degeneracy between the two transverse sheets of the slowness surface exists in directions of fourfold and sixfold (transverse isotropy) symmetry. Near an axis of transverse isotropy the pure transverse sheet of the slowness surface is convex and the quasitransverse sheet may be convex or concave, depending on the elastic constant ratios. In either case, along the axis $\tilde{G}_{33}$ exhibits a kink singularity and $\tilde{G}_{11}=\tilde{G}_{22}$ exhibit discontinuities.

At a fourfold axis, depending on the elastic constant ratios, $\tilde{G}_{11}=\tilde{G}_{22}$ exhibits either a discontinuity or a logarithmic type divergence, depending on the shape of the slowness surface in the region of the point of contact where the Gaussian curvature is not defined. We illustrate the possibilities by considering here the case of the [001] axis in cubic symmetry. Every[35] has described in detail the dependence of the shape of the slowness and wave surfaces of cubic media on the two elastic constant ratios C_{11}/C_{44} and C_{12}/C_{44}, and has established the thresholds $A,B,C,...$ at which structural changes occur in these surfaces near the ⟨100⟩ directions. Starting from a small value of the anisotropy, both transverse sheets of the slowness surface are convex and $\tilde{G}_{33}$ shows a kink and $G_{11}=G_{22}$ show discontinuities. With increasing C_{12}/C_{44} the threshold A is crossed at which wedges of saddle shape in the slow transverse (ST) sheet penetrate to the contact point. The direction of negative principal curvature in the wedges is circumferential with respect to the contact point, while the radial curvature, both inside and outside the wedges is positive. As a consequence the singularity displayed by $\tilde{G}_{11}=\tilde{G}_{22}$ remains a discontinuity which, however, becomes very large as threshold B is approached. Between the thresholds B and C, the radial curvature is negative in the [100] and [010] directions but still positive in the [110] and [1$\bar{1}$0] directions. In this elastic constant domain $\tilde{G}_{11}=\tilde{G}_{22}$ displays a logarithmic type divergence. Beyond the threshold C the radial curvature is negative in all directions and $\tilde{G}_{11}=\tilde{G}_{22}$ displays again a discontinuity. The circumferential curvature evidently plays no role in determining the nature of the singularity.

III. NUMERICAL EXAMPLES

A. Zinc

Figure 1 shows the (010) section of the group velocity (ray) surface of zinc. As a hexagonal crystal, zinc conforms to transverse acoustic isotropy, and the 3-D ray surface is generated by revolving this section about the [001] axis. The (010) and equivalent planes are mirror planes. The pure transverse (T) mode is polarized in the [010] direction, while the quasilongitudinal (qL) and quasitransverse (qT) modes are polarized in the (010) plane. The qT sheet has a circular fold encircling the [001] axis at an angle of 21.5°, which appears sectioned as the cusp (point 10) in Fig. 1. There is also a circular fold very close to the (001) plane but that is not well resolved in the diagram. At point 3 on the qT sheet, the ray surface is conical in shape. Lines *a*, *b*, *c*, and *d* denote directions for which calculated response functions are presented below.

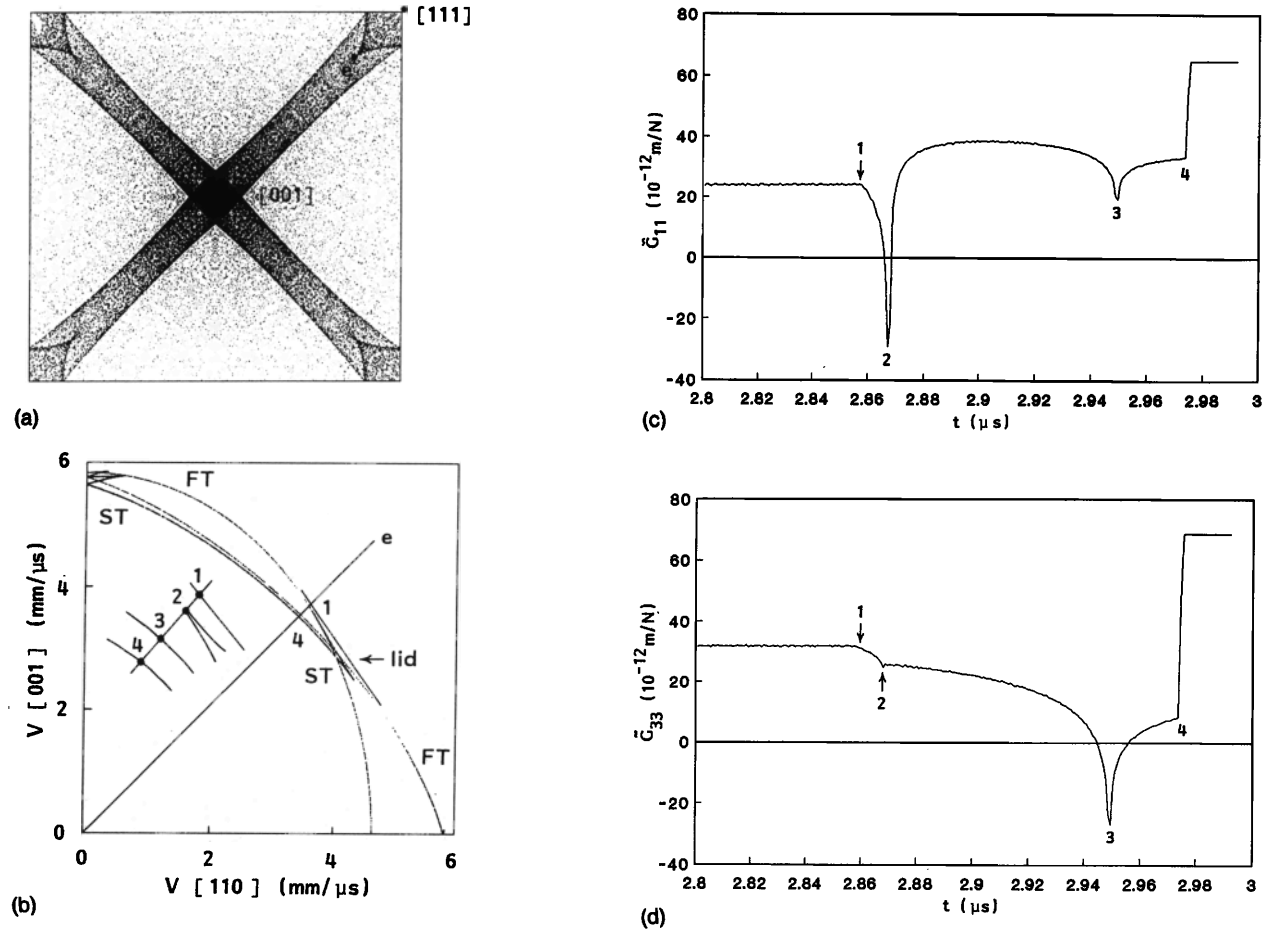

FIG. 6. (a) Focusing pattern of the ST modes of silicon. (b) A (110) section of the transverse sheets of the ray surface of silicon. The inset is a blow up of the region of the ray surface in the direction e. (c) $\tilde{G}_{11}$ and (d) $\tilde{G}_{33}$ for silicon in the direction e of the cusp. $\mathbf{x}=(7.6,7.6,10.0)$ in mm.

Figure 2(a) and (b) show the response functions $\tilde{G}_{33}$ and $\tilde{G}_{11}$ for direction a along the symmetry axis. The wave arrivals denoted 1, 2, and 3 correspond to the similarly numbered points on the ray section in Fig. 1. For $\tilde{G}_{33}$ there is a discontinuity at 1. It is fairly small because even though $\Lambda=1$, the Gaussian curvature of the L sheet of the slowness surface is fairly large in the region of the x_3 axis. There is a kink at 2 ($\Lambda=0$) and a strong $1/(-T)^{1/2}$ divergence followed by a discontinuity associated with the conical point 3. Regarding $\tilde{G}_{11}$, there is a kink at 1 ($\Lambda=0$), a small discontinuity at 2, and a $1/(-T)^{1/2}$ divergence followed by a discontinuity at 3. Because of the finite discretized time interval used in the calculations, the discontinuities appear as very rapid rather than sudden changes in $\tilde{G}$ in these figures.

Figure 3(a) and (b) show the response functions $\tilde{G}_{33}$ and $\tilde{G}_{22}$ in the direction b. For $\tilde{G}_{33}$ there is a discontinuity at 4 ($\Lambda\approx 1$), a change in slope and a barely visible discontinuity at 5 ($\Lambda\approx 0$), no singular feature at all is present at 6 ($\Lambda=0$ for all the T modes), there is a logarithmic divergence at 7 and a discontinuity at 8. For $\tilde{G}_{22}$ there is a kink at 4 ($\Lambda=0$), another kink at 5 ($\Lambda=0$), a discontinuity at 6 ($\Lambda=1$) with the pure T wave arrival, and kinks at 7 and 8 ($\Lambda=0$).

Figure 4(a), (b), and (c) show $\tilde{G}_{33}$, $\tilde{G}_{22}$, and $\tilde{G}_{11}$ in the direction c of the fold. At point 9 $\tilde{G}_{33}$ shows a discontinuity ($\Lambda\approx 1$), $\tilde{G}_{11}$ a small discontinuity ($|\Lambda|\ll 1$) and $\tilde{G}_{22}$ a kink ($\Lambda=0$). At the cusp point 10, $\tilde{G}_{33}$ shows a weak $1/|T|^{1/6}$ negative divergence ($|\Lambda|\ll 1$), $\tilde{G}_{11}$ shows a large $1/|T|^{1/6}$ negative divergence ($\Lambda\approx 1$), and $\tilde{G}_{22}$ a vertical slope (divergence in $\partial\tilde{G}/\partial T$) ($\Lambda=0$). At point 11 with the pure T wave arrival $\tilde{G}_{33}$ shows no singular features ($\Lambda=0$ for all T modes), $\tilde{G}_{22}$ shows a discontinuity ($\Lambda=1$) and $\tilde{G}_{11}$ shows a kink ($\Lambda=0$). At point 12 $\tilde{G}_{33}$ and $\tilde{G}_{11}$ display discontinuities and $\tilde{G}_{22}$ a kink ($\Lambda=0$). Figure 4(d) shows $\tilde{G}_{11}$ for the direction d, which lies slightly beyond the cusp. It is very similar to Fig. 4(c), except that at point 13 there is a deep but nonsingular minimum (see Sec. II E).

B. Diamond

Figure 5(a) shows a Monte Carlo calculated focusing pattern for the transverse modes of diamond in the vicinity of the [001] direction. It represents the distribution of ray vector directions corresponding to an isotropic distribution of slowness vectors. The resulting intensity is inversely proportional to the Gaussian curvature of the slowness surface. The elastic constant ratios of diamond place it in the domain between conditions A and B of Every.[35] The slow transverse (ST) mode displays caustics which straddle the (110) and (1$\bar{1}$0) planes and converge on the acoustic axis in the [001] direction, where the transverse mode slowness sheets make tangential contact. Figure 5(b) and (c) show the response functions $\tilde{G}_{33}$ and $\tilde{G}_{11}$ for this symmetry di-

rection. $\tilde{G}_{33}$ exhibits a discontinuity at the L wave arrival ($\Lambda=1$) and a kink at the arrival of the transverse waves ($\Lambda=0$). $\tilde{G}_{11}$ shows a kink at the L wave arrival ($\Lambda=0$) and a deep but finite minimum and discontinuity at the transverse wave arrivals. As condition B on the elastic constants is approached this minimum becomes progressively deeper and transforms into a logarithmic type divergence beyond the threshold B.

C. Silicon

Figure 6(a) shows the ST focusing pattern of silicon centered on the [001] direction and extending at the corners to the ⟨111⟩ directions. Figure 6(b) shows the symmetry plane (110) section of the slow (ST) and fast (FT) transverse sheets of the ray surface of silicon. Figure 6(c) and (d) show $\tilde{G}_{11}$ and $\tilde{G}_{33}$ for silicon in the region of the transverse wave arrivals for the direction denoted e in 6(a) and 6(b), which coincides with a cusp in the ST sheet, and which passes through a circular lid in the wave surface associated with the conical point in the [111] direction. There are four wave arrivals denoted 1 (the lid), 2 (the ST cusp), 3 (associated with a saddle-shaped portion of ST sheet of slowness surface), and 4 (convex portion of ST sheet). For $\tilde{G}_{11}$ there is a kink at 1, a $1/|T|^{1/4}$ divergence at 2, a logarithmic divergence at 3, and a discontinuity at 4. For $\tilde{G}_{33}$ there is a kink at 1, a vertical slope at 2 ($\Lambda=0$), a logarithmic divergence at 3, and a discontinuity at 4.

IV. COMPARISON WITH EXPERIMENT

We compare here computed response functions for silicon and zinc with waveforms measured in silicon and zinc single crystals using the capillary fracture technique.[36] In this method the sharp edge of a razor blade is pressed down with steadily increasing force on a fine glass capillary lying on the surface of a sample. At the instant the capillary fractures there is an abrupt change in the normal force acting on the surface of the sample. The normal displacement at a point on the opposite surface in response to this change in force is measured using a small aperture capacitive detector. We compare below the voltage signal from the capacitive detector, which is proportional to the normal component of the displacement of the sensed surface, with the computed displacement response function for the infinite elastic continuum. The data pertains to early times prior to the arrival of reflected waves, and to directions not too far removed from epicenter so that head wave effects are not pronounced. Under these conditions the infinite continuum response functions are in overall good agreement with the measured waveforms, particularly with regard to the arrival times of the various singular features and their relative magnitudes. Naturally because of the small but finite rise time of the force ($\approx 0.1\ \mu s$), the finite bandwidth of the signal processing circuitry and the small but finite sizes of the force and sensing areas, there is some rounding of the measured data as compared with the computed response functions. Taking the x_3 axis to be the inward normal at the sample's surface, it is the component $\tilde{G}_{33}(\mathbf{x},t)$ of the response function with which the comparison is made.

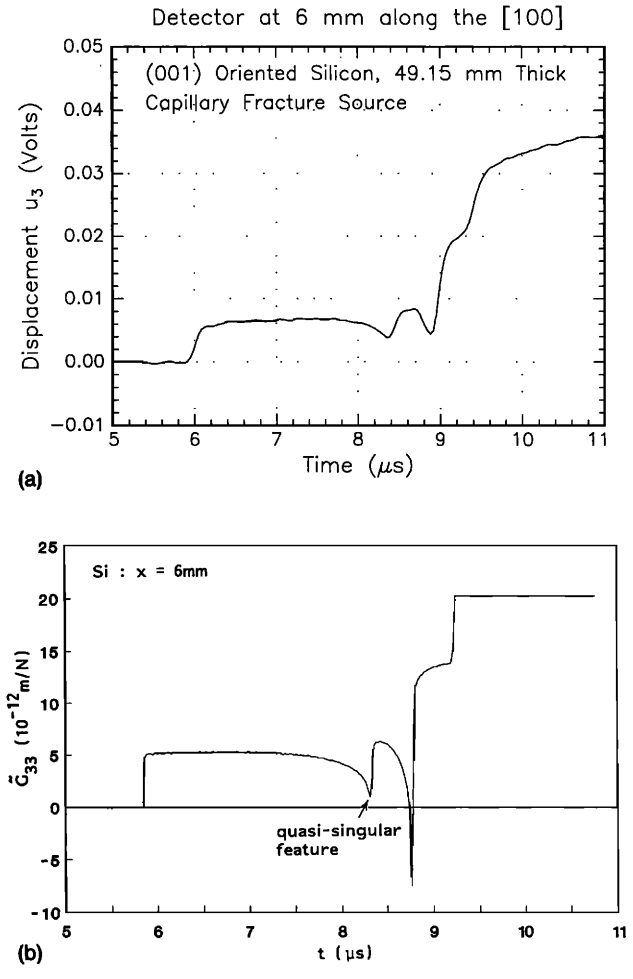

FIG. 7. (a) Measured waveform and (b) corresponding calculated $\tilde{G}_{33}(x,t)$ for silicon. $\mathbf{x}=(6.0,0,49.15)$ in mm.

Figure 7(a) and (b) show the measured waveform and corresponding computed response function $\tilde{G}_{33}(\mathbf{x},t)$, respectively, for a (001) oriented silicon crystal of thickness 49.15 mm, with detection at a point located 6 mm from epicenter in the [100] direction. There is good agreement between the two with regard to all the prominent features, the discontinuity at the L wave arrival and the two sharp minima, shoulder and discontinuity at the T wave arrivals. We have carried out computer simulations in which the change in the force is treated not as instantaneous but spread over a short time interval, and these give good account of the rounding of the singular features in the experimental waveform. The quasisingular feature is a deep minimum that arises from the fact that the sensing direction x lies slightly outside a fold in the ST sheet of the wave surface. The second deep minimum, on expansion of the time scale, resolves into a closely spaced logarithmic divergence and large discontinuity. This feature is due to the sensing direction lying slightly inside of another fold in the ST sheet of the wave surface. A more extensive comparison between theory and experiment on the dynamical response of Si will be presented elsewhere.

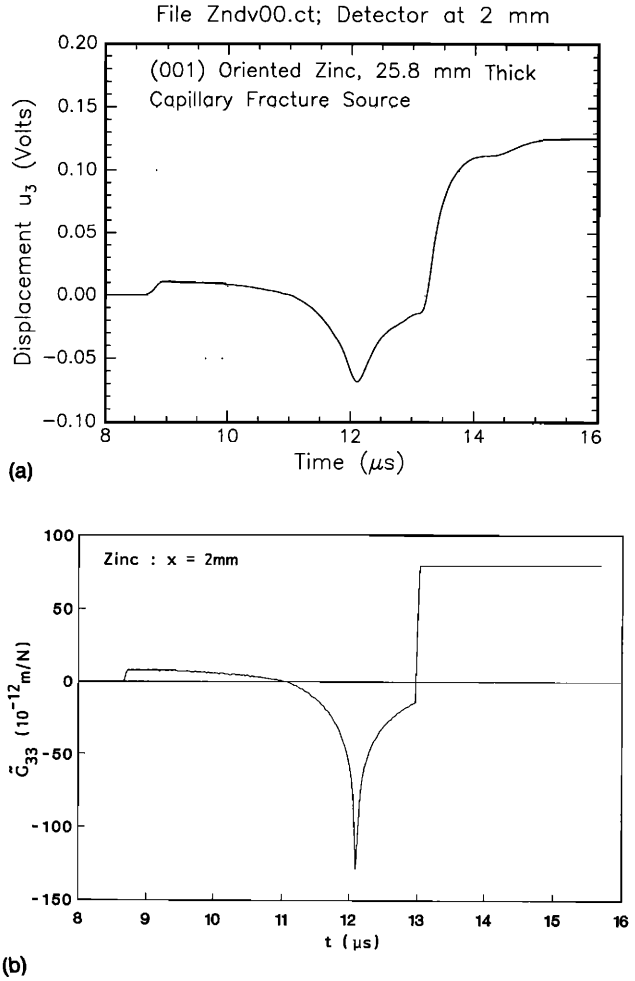

FIG. 8. (a) Measured waveform and (b) corresponding calculated $\tilde{G}_{33}(x,t)$ for zinc. $\mathbf{x}=(2.0,0,25.8)$ in mm.

Figure 8(a) and (b) show the measured waveform and corresponding computed response function $\tilde{G}_{33}(\mathbf{x},t)$, respectively, for a [0001] oriented zinc single crystal of thickness 25.8 mm, with detection at a point located 2 mm from epicenter. There is good agreement between the two with regard to all the main features, the discontinuity at the L wave arrival, the barely noticeable kink, which in practice looks smooth, at the first qT wave arrival, the logarithmic divergence at the second qT wave arrival and the discontinuity at the last qT wave arrival. There is no singular feature at all coinciding with the pure T wave arrival, for reasons discussed earlier. The slight dip in the measured waveform immediately preceding the last qT wave arrival is associated with a head wave.[37] Kim *et al.*[7] have reported observation of the strong focusing associated with the $1/|T|^{1/2}$ singularity on the symmetry axis of Zn.

V. CONCLUSIONS

The method described here for calculating the dynamic response of an infinite elastic continuum to a concentrated point force with Heaviside step function time dependence is simple and expedient. The relevant computer coding is easily implemented, and the CPU time required in the calculations is modest. The programs are easily adapted to extended source and detector and finite rise time of the force, with the ensuing increase in computer time being negligible.

A prominent feature of these response functions are the singularities (sharp features) they display at wave arrivals. This has been a principal focus of this paper, and we have identified a number of new singularity types. We have drawn attention to the influence that symmetry has on wave arrival singularities. Through a number of numerical examples we have illustrated the occurrence of these singularities in the response functions of actual materials. These singularities survive in the response functions of elastic half-spaces, plates, and other bounded geometries, and are thus useful entities on which to anchor the interpretation of experimental data obtained on finite test specimens.

Comparison has been made between computed response functions and waveforms measured in silicon and zinc crystals using the capillary fracture technique. For data pertaining to first arrivals, and in directions in which head wave effects are not pronounced, there is good agreement between theory and experiment, particularly with regard to the various singular features that are present.

ACKNOWLEDGMENTS

A.G.E. thanks the Foundation for Research Development for continuing financial support. K.Y.K. acknowledges support from the Office of Naval Research.

[1] For a review see: G. A. Northrop and J. P. Wolfe, in *Nonequilibrium Phonon Dynamics*, edited by W. E. Bron (Plenum, New York, 1985), p. 165.
[2] A. G. Every, W. Sachse, K. Y. Kim, and M. O. Thompson, Phys. Rev. Lett. **65**, 1446 (1990).
[3] A. G. Every and W. Sachse, Phys. Rev. B **44**, 6689 (1991).
[4] M. R. Hauser, R. L. Weaver, and J. P. Wolfe, Phys. Rev. Lett. **68**, 2604 (1992).
[5] R. L. Weaver, M. R. Hauser, and J. P. Wolfe, Z. Phys. B **90**, 27 (1993).
[6] J. Wesner, K. U. Wurz, K. Hillmann, and W. Grill, in *Phonon Scattering in Condensed Matter VII*, edited by M. Meissner and R. O. Pohl, Springer Series in Solid State Sciences, Vol. 112 (Springer-Verlag, New York, 1993), p. 68.
[7] K. Y. Kim, W. Sachse, and A. G. Every, Phys. Rev. Lett. **70**, 3443 (1993).
[8] K. Y. Kim, A. G. Every, and W. Sachse, J. Acoust. Soc. Am. (to be published).
[9] A. A. Kolomenskii and A. A. Maznev, JETP Lett. **53**, 423 (1991).
[10] G. F. D. Duff, Philos. Trans. R. Soc. London **252**, 249 (1960).
[11] R. G. Payton, *Elastic Wave Propagation in Transversely Isotropic Media* (Martinus Nijhoff, The Hague, 1983).
[12] A. G. Every, K. Y. Kim, and W. Sachse, *Proceedings of the 29th Polish Winter School in Theoretical Physics*, edited by T. Paszkiewicz and K. Rapcewicz (Plenum, New York, in press).
[13] V. T. Buchwald, Proc. R. Soc. London Ser. A **253**, 563 (1959).
[14] R. Burridge, Q. J. Mech. Appl. Math. **20**, 41 (1967).
[15] N. Cameron and G. Eason, Q. J. Mech. Appl. Math. **20**, 23 (1967).
[16] F. R. Yeatts, Phys. Rev. B **29**, 1674 (1984).
[17] J. H. M. T. van der Hijden, *Propagation of Transient Elastic Waves in Stratified Anisotropic Media* (North-Holland, Amsterdam, 1987).
[18] M. G. Cottam and A. A. Maradudin, in *Surface Excitations*, edited by V. M. Agranovich and R. Loudon (Elsevier, Amsterdam, 1984), p. 1.
[19] V. K. Tewary and C. M. Fortunko, J. Acoust. Soc. Am. **91**, 1888 (1992).
[20] A. Tverdokhlebov and J. Rose, J. Acoust. Soc. Am. **83**, 118 (1988).
[21] H. Zhu, ASME J. Appl. Mech. **59**, 596 (1992).
[22] C. Y. Wang and J. D. Achenbach, Wave Motion **6**, 389 (1992).

[23] K. Aki and P. Richards, *Quantitative Seismology* (Freeman, San Francisco, 1980).
[24] A. N. Ceranoglu and Y. H. Pao, J. Appl. Mech. **48**, 125, 133, 139 (1981).
[25] R. Burridge, P. Chadwick, and A. N. Norris, Proc. R. Soc. London Ser. A **440**, 655 (1993).
[26] R. G. Payton, Q. J. Mech. Appl. Math. **45**, 183 (1992).
[27] L. van Hove, Phys. Rev. **89**, 1189 (1953).
[28] D. M. Barnett, Phys. Status Solidi **49**, 741 (1972).
[29] H. J. Maris, J. Acoust. Soc. Am. **50**, 812 (1971).
[30] V. I. Alshits, A. V. Sarychev, and A. L. Shuvalov, Sov. Phys. JETP **62**, 531 (1985).
[31] H. J. Maris, Phys. Rev. B **28**, 7033 (1983).
[32] M. V. Berry, Adv. Phys. **25**, 1 (1976).
[33] A. G. Every, Phys. Rev. B **34**, 2852 (1986).
[34] P. A. Barry and M. J. P. Musgrave, Q. J. Mech. Appl. Math. **32**, 205 (1979).
[35] A. G. Every, Phys. Rev. B **24**, 3456 (1981).
[36] K. Y. Kim, L. Niu, B. Castagnede, and W. Sachse, Rev. Sci. Instrum. **60**, 2785 (1989).
[37] R. L. Weaver, W. Sachse, and K. Y. Kim (to be published).